

See discussions, stats, and author profiles for this publication at: <https://www.researchgate.net/publication/379466130>

# A data-driven framework to improve the wear resistance of a low-alloy steel fabricated by laser powder bed fusion

Article in *Journal of Manufacturing Processes* · April 2024

DOI: 10.1016/j.jmapro.2024.01.083

CITATIONS

2

10 authors, including:



Jiahui Zhang

University of Toronto

9 PUBLICATIONS 97 CITATIONS

SEE PROFILE



Zhiying Liu

University of Toronto

28 PUBLICATIONS 516 CITATIONS

SEE PROFILE

READS

76



Sagar Patel

Nikon SLM Solutions

25 PUBLICATIONS 280 CITATIONS

SEE PROFILE



Wandong Wang

University of Toronto

6 PUBLICATIONS 46 CITATIONS

SEE PROFILE



# A data-driven framework to improve the wear resistance of a low-alloy steel fabricated by laser powder bed fusion

Jiahui Zhang<sup>a</sup>, Sagar Patel<sup>b</sup>, Zhiying Liu<sup>a</sup>, Tianyi Lyu<sup>a</sup>, Yuhao Wang<sup>a</sup>, Yujie Hua<sup>a</sup>, Wandong Wang<sup>a</sup>, Jason Hattrick-Simpers<sup>a</sup>, Mihaela Vlasea<sup>b</sup>, Yu Zou<sup>a,\*</sup>

<sup>a</sup> Department of Materials Science and Engineering, University of Toronto, Toronto, ON M5S 3E4, Canada

<sup>b</sup> Department of Mechanical and Mechatronics Engineering, University of Waterloo, Waterloo, ON N2L 3G1, Canada

## ARTICLE INFO

### Keywords:

Laser powder bed fusion  
Parameter optimization  
Data-driven framework  
Relative density  
Wear resistance

## ABSTRACT

The laser powder bed fusion (LPBF) technique provides an opportunity to precisely control process parameters and produce materials with desired microstructure, which play an important role in developing wear-resistance components. An accurate and efficient determination of the optimal process window for new materials, however, remains a highly sought yet challenging task due to a high experimental cost by trial and error. In this study, we demonstrate a physics-informed data-driven framework to create a 3D process map and optimize printing parameters (i.e., laser power ( $P$ ), scan speed ( $v$ ), and hatch distance ( $h$ )) for a newly designed low-alloy steel. First, we establish a highly precise  $P$ - $v$  process map by thoroughly exploring kernel selection and parameter hyper-tuning in Gaussian process regression (GPR) models. Subsequently, we employ the Bayesian optimization (BO) algorithm with different exploration-exploitation trade-offs to automatically explore all feasible optimized printing recipes within the process map. To efficiently incorporate a third printing parameter ( $h$ ) alongside  $P$  and  $v$  with limited additional data points, we integrate a physics-informed pre-analysis and an inverse design strategy. We show that the samples fabricated by our optimized parameters exhibit improvement in relative density and retain a high hardness, resulting in a superior wear rate compared to those produced using non-optimized parameters. Furthermore, our samples outperform LPBF-fabricated steels and metal matrix composites in the literature, which is attributed to the existence of oxidative and fatigue wear. Our study offers a systematic and accurate data-driven approach to design and optimize microstructures and properties of materials made by LPBF.

## 1. Introduction

Wear is a major cause of material wastage and degradation of mechanical performance, resulting in significant economic losses [1–3]. Increasing the hardness and relative density are two main strategies to improve the friction and tribology properties of materials [4,5]. Laser powder bed fusion (LPBF), known for its rapid cooling characteristics, has the potential to print components with finer grain sizes, leading to improved hardness compared to traditional fabrication methods [6,7]. To fully leverage the advantages of LPBF, determining optimal processing windows is essential but challenging because there are multiple printing parameters, such as powder quality, laser power, scan speed, and hatch distance, that can impact the hardness and relative density of the fabricated part [8–10]. For a newly-designed material, establishing the parameter-property relationship typically relies on multiple rounds of design of experiment (DOE) and trial-and-error, which are laborious

and costly [11]. Therefore, an efficient and robust method to optimize the printing recipes and customize microstructure response to tailor material properties is highly desirable. A printing recipe is defined herein as a combination of processing parameters used to produce a component.

Recently, machine learning (ML) methods have shown promise in discovering optimized processing windows [12–16]. For instance, Liu et al., [17] developed a GPR model with a default kernel and hyper-parameter to identify a new and much larger  $P$ - $v$  window for manufacturing fully dense LPBF AlSi10Mg. He et al., [18] used the same GPR model to establish an optimized  $P$ - $v$  window for high density of TiCN-reinforced AlSi10Mg. However, it is worth noting that the accuracy of the established process map could be further improved with appropriate kernel selection and parameter hyper-tuning. The improvement in model accuracy can lead to more precise predictions and better optimization outcomes. Moreover, their approach was limited to the man-

\* Corresponding author.

E-mail address: [mse.zou@utoronto.ca](mailto:mse.zou@utoronto.ca) (Y. Zou).

<https://doi.org/10.1016/j.jmapro.2024.01.083>

Received 3 August 2023; Received in revised form 7 November 2023; Accepted 31 January 2024  
1526-6125/© 20XX

ual selection of optimized printing recipes within the predicted high relative density regions of the process map. Consequently, their optimized samples did not demonstrate an improvement in mechanical properties. Additionally, incorporating a third printing parameter alongside  $P$  and  $v$  to establish a 3D processing window multiplies the data point requirements and introduces ambiguity in the design strategy for constructing a GPR model.

In this study, we demonstrate a data-driven framework for optimizing the printing recipe to target high-density outcomes and designing a desired level of wear resistance for LPBF low-alloy steel parts. To establish a 3D process map, 42 different recipes are generated by normalizing the three dominant LPBF printing parameters: laser power ( $P$ ), scan speed ( $v$ ), and hatch distance ( $h$ ), into dimensionless inputs. We perform a thorough investigation of GPR models, including the choices of kernels and various related hyperparameters, to establish a precise  $P$ - $v$  processing window. Subsequently, different active learning strategies of the Bayesian optimization (BO) algorithm are employed to automatically search for globally optimal processing parameters for denser samples. Additionally, to determine hatch distance for desired low relative density samples, a combination of physical-informed pre-analysis and inverse design strategy is used. We tested and compared the mechanical properties of nine samples printed by selected recipes and demonstrated that the samples fabricated by optimized parameters possessed improved mechanical properties. Our work proposes a novel and readily applicable methodology based on LPBF process physics and machine learning to optimize the printing recipes and design desired properties.

**Table 1**

The chemical composition of the modified water atomized low-alloy steel powder measured using LECO analysis (all in wt%).

| Fe   | Mn  | Mo  | C     | S     | O     |
|------|-----|-----|-------|-------|-------|
| Bal. | 0.2 | 0.8 | 0.601 | 0.014 | 0.056 |

## 2. Materials and methods

### 2.1. Powder material and LPBF process

In this study, a modified water-atomized low-alloy steel powder with a D50 of 37.5  $\mu\text{m}$  (Rio Tinto QMP, Sorel-Tracy, QC, Canada) was used. The composition of the powder was measured using LECO analysis, as shown in Table 1. The scanning electron microscope (SEM) image, particle size distribution, and sphericity of the powder were characterized, as shown in Fig. 1(c–d).

All the specimens were fabricated by a commercial LPBF system (EOS M290, EOS GmbH, Germany) at room temperature with oxygen content under 100 ppm. To determine the printing recipes, a multiple-round design of experiments (DOE) was performed using a normalized process map, which incorporates dimensionless heat input ( $E^*$ ), dimensionless beam velocity ( $v^*$ ), and dimensionless hatch distance ( $h^*$ ) instead of directly selecting LPBF processing parameters [19,20], as shown in Fig. 1(a). The terms  $E^*$ ,  $v^*$ , and  $h^*$  are calculated from the following Eqs. (1), (2), and (3) respectively:

$$E^* = \frac{q^*}{l^*} = \frac{AP_{eff}}{2l_r\lambda(T_m - T_0)} \quad (1)$$

$$v^* = \frac{vr_b}{\alpha} \quad (2)$$

$$h^* = \frac{h}{r_b} \quad (3)$$

where  $A$  is the laser absorptivity,  $P$  laser power [W],  $l_r$  powder layer thickness [m],  $\lambda$  thermal conductivity [W/(mK)],  $T_m$  melting temperature [K],  $T_0$  substrate temperature [K],  $v$  laser beam velocity [m/s],  $r_b$  beam spot radius [m],  $\alpha$  thermal diffusivity [m<sup>2</sup>/s], and  $h$  the hatch distance [m]. In total, 42 recipes were chosen within the practical design space of the LPBF system, as illustrated in Fig. 1(b). For the LPBF system used, the beam spot radius at the focal point ( $r_b$ ) is given by 40  $\mu\text{m}$ , which was kept constant for this study. The experimental design was

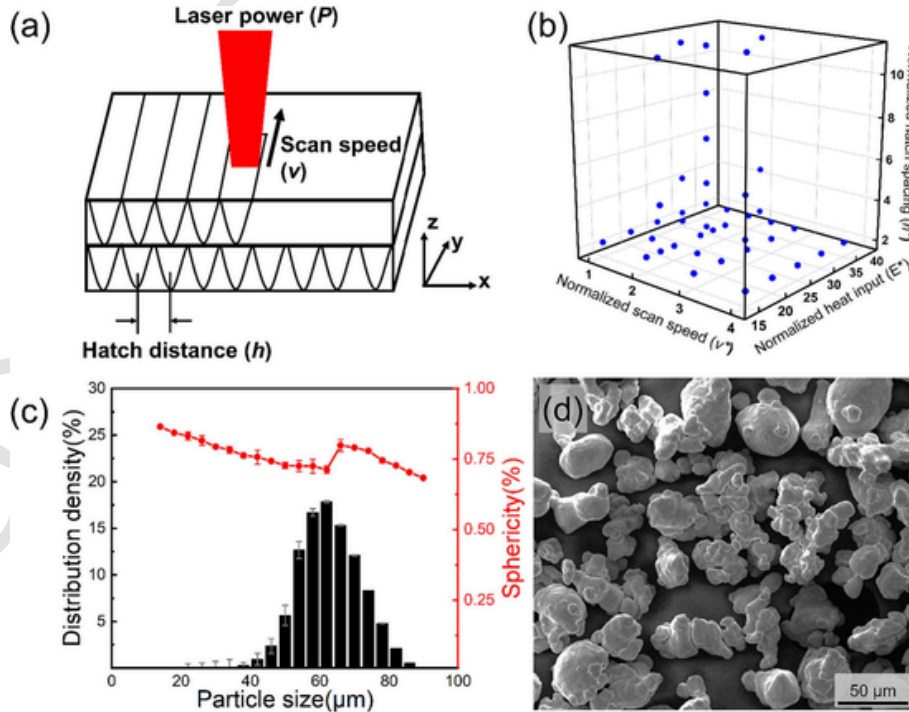


**Fig. 1.** The (a) schematic diagram of different printing parameters for the LPBF process and (b) data cloud representing the recipes chosen based on different normalized heat input ( $E^*$ ), normalized scan speed ( $v^*$ ), and normalized hatch distance ( $h^*$ ). The (c) particle size distribution and sphericity and (d) SEM image of the modified water atomized low-alloy steel powder used in this study. The low quality of water atomized metal powder results in poor reproducibility of experimental results.

undertaken entirely using the  $E^*$ ,  $v^*$ , and  $h^*$  terms, from which values for the laser power, beam velocity, and hatch distance were obtained. The laser absorptivity,  $A$ , values chosen for a given set of processing parameters in Eq. (1) are obtained from Eq. (4), which is an adaptation of the scaling law for laser absorptivity determined by Ye et al., for low reflectivity Ti, Fe, and Ni alloys using the terms described in. The term,  $q_m^*$ , in Eq. (4) is obtained by replacing the  $A$  term in Eq. (1) with  $A_m$  (the minimum melt absorptivity). The minimum melt absorptivity,  $A_m$ , value for ferrous alloys is reported as 0.28 by Ye et al., [21]. Which is used in this work.

$$A = 0.7 \left( 1 - \exp \left( -\frac{0.66q_m^*}{\pi v^*} \right) \right) \quad (4)$$

$E^*$  ranges from 15 to 35, corresponding to an approximate power range of 100–350 W, which reaches the general stable power limitation of the printer. To avoid issues such as lack of fusion, balling, or severe spattering, we selected a  $v^*$  range of 1 to 4 (corresponding to an approximate velocity range of 0.3–1.32 m/s), based on high-density data points from other ferrous alloys in LPBF literature. For  $h^*$ , the value varies from 2 to 11. A layer thickness of 40  $\mu\text{m}$  and an inter-layer rotation scanning strategy of 67° with a meander scanning strategy were employed. Values for the material constants used were calculated from Thermocalc software (TCFE10) and are summarized in Table 2.

## 2.2. Data-driven framework

In this study, a data-driven framework with Gaussian process regression (GPR), Bayesian optimization (BO), and inverse design strategy was proposed to establish the process map between printing parameters and relative density. BO with GPR as the objective function was used to find the optimized printing recipes of  $E^*$  and  $v^*$ , resulting in higher relative density samples. Subsequently, an inverse design strategy was employed to predict the corresponding  $h^*$  values for low relative density samples, thereby upgrading a 2D map to a comprehensive 3D map.

BO is a sequential design strategy for the global optimization of black-box functions, typically used to optimize expensive-to-evaluate functions [22]. Two main functions were employed to approach global extrema: (1) the surrogate function served as an approximation of the object function to be optimized based on the data points. (2) the acquisition function was used to propose sampling points in the design space, balancing exploitation and exploration [23]. In this study, the GPR model was used as the surrogate function to establish the relationship between processing parameters and relative densities of the fabricated components [24]. The function can be sampled at a specific printing parameter according to:

$$RD(E^*, v^*) \sim GP \left( m(E^*, v^*, h^*), k(E^*, v^*, h^*, E^{*'}, v^{*'}, h^{*'}) \right) \quad (5)$$

where  $RD(E^*, v^*, h^*)$  is the relative density we sample from the GP,  $m(E^*, v^*, h^*)$  is the mean function, and  $k(E^*, v^*, h^*, E^{*'}, v^{*'}, h^{*'})$  is the covariance function, which is a subclass of kernel functions. The power of the Gaussian process to express a wide range of functions rests solely on

the shoulders of the covariance function (kernel). Of all the covariance functions, the squared exponential (SE) kernel, also known as the radial basis function (RBF) kernel, is often the default choice for GPR. The RBF kernel is expressed as follows:

$$k(x_i, x_j) = \exp \left( -\frac{d(x_i, x_j)^2}{2l^2} \right) \quad (6)$$

where  $l$  is the length scale of the kernel and  $d(x_i, x_j)$  is the Euclidean distance. Matérn Kernel, a generation of the RBF Kernel, has an additional parameter  $\nu$ , to control the smoothness of the resulting function, given by:

$$k(x_i, x_j) = \frac{1}{\Gamma(\nu) 2^{\nu-1}} \left( \frac{\sqrt{2\nu}}{l} d(x_i, x_j) \right)^\nu \times K_\nu \left( \frac{\sqrt{2\nu}}{l} d(x_i, x_j) \right) \quad (7)$$

where  $d(x_i, x_j)$  is the Euclidean distance,  $K_\nu$  is a modified Bessel function, and  $\Gamma(\nu)$  is the gamma function. Moreover, we selected rational quadratic (RQ) kernel, which could be regarded as a scale mixture of RBF kernels with different characteristic length scales and is given by:

$$k(x_i, x_j) = \left( 1 + \frac{d(x_i, x_j)^2}{2\alpha l^2} \right)^{-\alpha} \quad (8)$$

where  $\alpha$  is the scale mixture parameter. In this study, we employed a constant kernel as part of a product kernel to modify the mean of the Gaussian process. The acquisition functions, which are used to construct a utility function from the model posterior and direct the sampling towards areas where an improvement over the current best observation is likely, are updated from the prior. The upper confidence bound (UCB) was adopted as the acquisition function in this study, which was developed to exploit lower confidence bounds that minimize regret over the course of optimization. The UCB acquisition function is shown as follows:

$$a_{UCB}(x) = \mu(x) + \lambda \sigma(x) \quad (9)$$

where  $\lambda > 0$  is a trade-off parameter and  $\sigma(x) = \sqrt{k(x_i, x_j)}$  is the marginal standard deviation of GPR.

## 2.3. Microstructure characterization and mechanical testing

Low-alloy steel cylinders ( $\Phi 5 \times 10 \text{ mm}^3$ ) and cubes (10 mm edge length) were printed based on all recipes in our dataset and porosity (for all cylinders) was measured using a 3D X-ray computed tomography (XCT) scanner (ZEISS Xradia 520 Versa) with a 5.5  $\mu\text{m}$  voxel size. The defect distribution within each sample was visualized using an image processing software (Dragonfly 3.0, Object Research Systems Inc., Montreal, QC) to segment and visualize the pore space; pores with an aspect ratio  $> 0.7$  were considered as “rounded defects” and pores with an aspect ratio  $< 0.7$  were considered to be irregular-shaped defects. Three selected samples were mounted, mechanically grounded with 600, 800, and 1200 grit sandpapers, followed by 1  $\mu\text{m}$  chromium oxide green suspension, and finally vibratory polished for 15 mins using a 20 nm colloidal silica. Microstructures and element distribution were analyzed using a SEM (Hitachi 3500) equipped with energy dispersive spectrometer (EDS). Electron backscatter diffraction (EBSD) characterization with an accelerating voltage of 20 KV and step size of 250 nm was applied to investigate the grain size and crystallographic orientation.

**Table 2**  
Thermophysical properties of the low-alloy steel used in this work.

| Properties                      | Values |
|---------------------------------|--------|
| Density [kg/m <sup>3</sup> ]    | 7758   |
| Thermal conductivity [W/(m.K)]  | 55.34  |
| Specific heat capacity [J/kg.K] | 482    |
| Melting temperature [K]         | 1758   |
| Vaporization temperature [K]    | 3070   |

The mechanical properties of select samples were characterized by hardness tests and tribological tests. The hardness was measured by a Vickers hardness tester according to ASTM E92 standard [25], with an applied load of 200 g and dwelling time of 10s. The tribological tests were conducted on a ball-on-disk tribometer (MFT-5000, Rtec) to analyze the friction characteristics of cubic low-alloy steel samples with dimensions of  $10 \times 10 \times 10 \text{ mm}^3$ , following the ASTM G133–05 standard [26]. A WC-Co ball (Hardness: 90–92 HRC) with a quarter inch diameter was used as the counterpart with a normal load of 50 N, sliding distance of 8 mm, sliding speed of 8 mm/s, and sliding duration of 1 h. Duplicate tests were performed for repeatability, and wear volumes ( $\text{mm}^3$ ) were calculated by measuring average cross-sectional area of wear tracks multiplied by the wear track length. The worn surfaces were visualized by Stylus Profiler (Alpha-Step D-500) and 12 different wear depth profiles were measured for each wear track.

### 3. Results

#### 3.1. Importance of processing parameters on density

Compared with the commonly used Archimedes method [27] and optical microscope images analysis [28] for density characterization, XCT technology yields more accurate results when measuring high-density samples with an adequate voxel size resolution. In this study, the relative densities of all the specimens were calculated by considering all the defects comprised of a cluster of 4 or more voxels, to reduce the impact of noise in XCT data. To minimize experimental error, two duplicates of each sample were fabricated. However, due to the irregular characteristic of water-atomized powders, as well as the spatial distribution of specimen replicates across the build plate, there was a noticeable discrepancy in the relative densities of the duplicate samples. Fig. 2 demonstrates the relationship between processing parameters and relative densities. Among the controlled parameters, it is evident that the relative density is most sensitive to changes in  $h^*$ , decreasing from 99 % to 75 % with the increase of  $h^*$  from 2 to 11, as shown in Fig. 2(b). For the LPBF printing process, a higher hatch distance means a larger gap between two consecutive scans, resulting in a decrease of the energy input, which leads to incomplete melting of metal powders [29]. Furthermore, the influence of  $E^*$  and  $v^*$  on relative density is weaker yet more complicated when  $h^*$  is fixed at 2.22, as illustrated in Fig. 2(a).

#### 3.2. $E^*$ & $v^*$ -density contour map by GPR models

In this study, considering the small size of the dataset and the dominant impact of  $h^*$ , a combination of the 2D GPR model and BO was used to construct the  $E^*$  &  $v^*$ -density contour map and optimize the printing recipe for higher relative density samples. Afterward, the inverse design strategy was employed to identify the  $h^*$  value corresponding to the desired low-density samples.

To establish the 2D map, data points from two rounds of DOEs were selected, with  $h^*$  fixed at 2.22. In DOE #1,  $E^*$  ranges from 15 to 35 in intervals of 5 and  $v^*$  ranges from 1 to 4 in intervals of 1, resulting in 20 combinations based on grid search. In DOE #2, 8 new combinations of parameters are selected around the highest relative density recipe obtained in DOE #1 within the parameter range, using a central composite design methodology with  $h^*$  fixed at 2.22, as demonstrated in Table S1. To select and hyper-tune the kernel functions for GPR models, the DOE #1 results were used as the training dataset and the model accuracy was evaluated by the root mean squared error (RMSE) of the DOE #2 results. The final GPR models were established based on DOE #1 data points, with the hyper-tuned RBF kernel (length-scale: [0.9,0.1]), the hyper-tuned Matérn kernel (nu:18, length-scale: [0.8,0.9]), and the hyper-tuned RQ kernel (Alpha: 6, length-scale: 0.5), respectively, as shown in Fig. 3(a1–c1). The RMSEs of RBF, Matérn, and RQ kernels are 0.136, 0.136, and 0.3589, respectively. When comparing RBF kernel with Matérn kernel, the latter one is more confident in its predicted relative density, indicated by a lower predicted standard deviation (STD), as shown in Fig. 3(a2–c2). The predicted relative density and STD of the DOE #2 recipes based on three models were compared with experimental validations, as demonstrated in Fig. 3(a3–c3). It is apparent that the relative densities predicted by the RBF model and the Matérn model agree better with the ground truth compared to RQ model.

#### 3.3. Processing parameter optimization and inverse design

Based on the established GPR model with RBF kernel, BO was conducted to search for the optimized printing recipes resulting a higher relative density. With the UCB acquisition function, the exploitation vs. exploration trade-off is straightforward and convenient to tune via the parameter  $\lambda$ . A smaller  $\lambda$  prioritizes high-performing solutions, while a larger  $\lambda$  encourages the exploration of unexplored areas in the research space. In this study, three different  $\lambda$  values were selected: 0, 1, and 10 for finding the next printing recipe to get rid of local maxima. When the  $\lambda$  is selected as 0, the optimized recipe will be selected en-

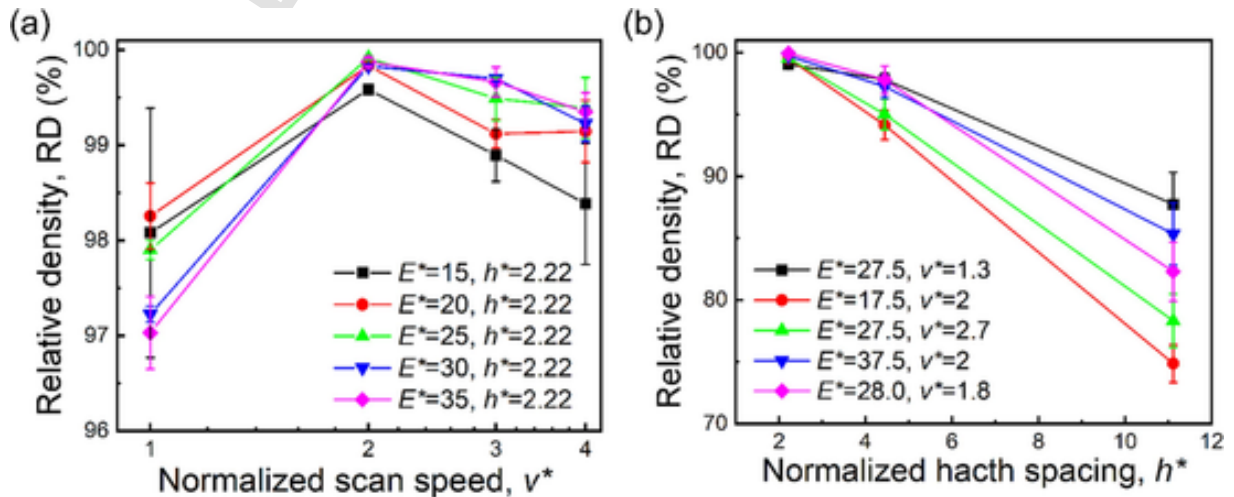
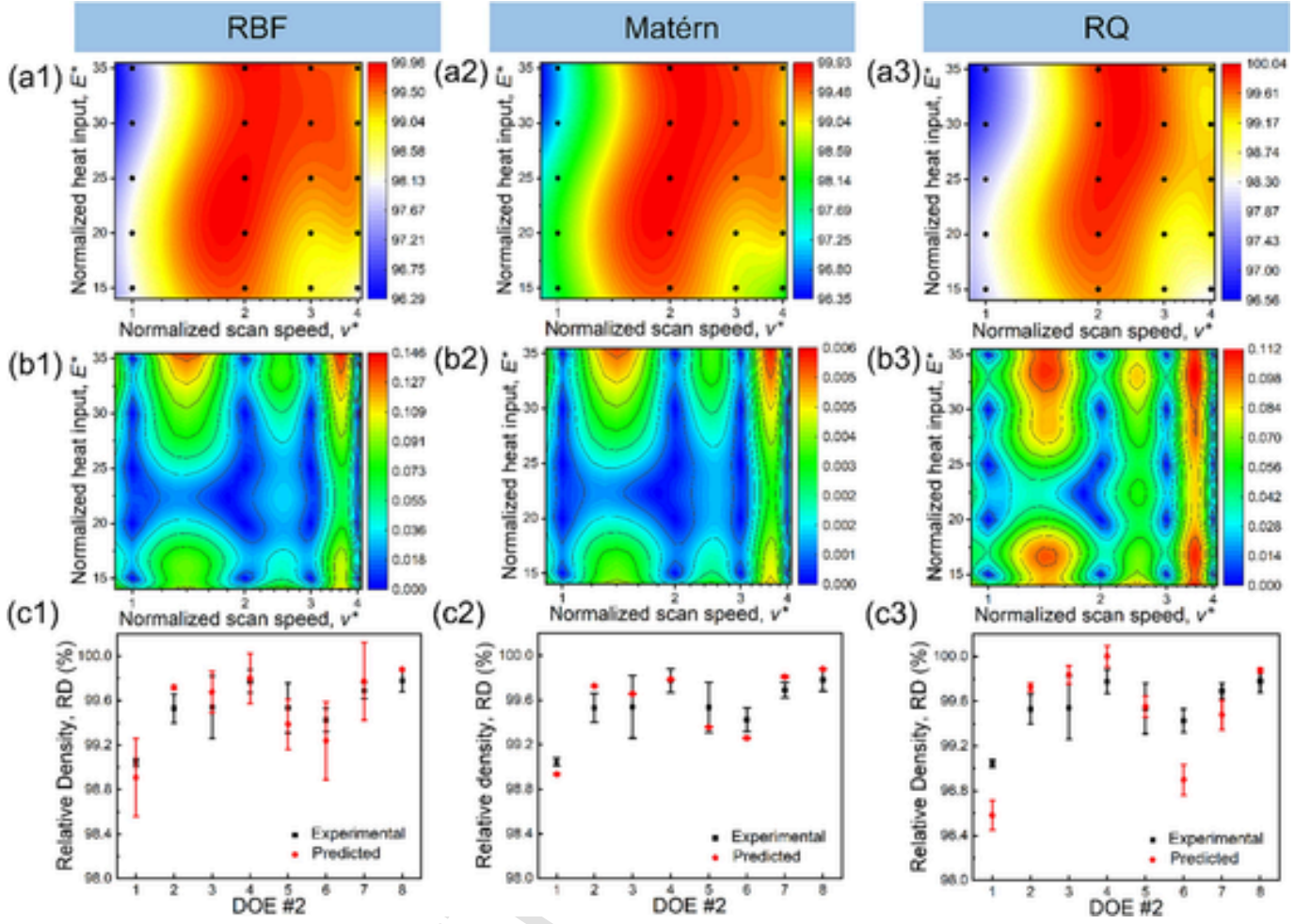


Fig. 2. The influence of (a) dimensionless input energy density,  $E^*$  and dimensionless scan speed,  $v^*$  and (b) dimensionless hatch distance,  $h^*$  on the relative density of printed components. The impact of  $h^*$  on relative density is more dominant than that of the other two factors. The increase in hatch spacing results in wider gaps between melt tracks, which may lead to the formation of inter-track pores.





**Fig. 3.** The (a1–a3) 2D process map, (b1–b3) confidence intervals, and (c1–c3) validation results based on DOE #2 data points predicted by the established Gaussian process regression models with RBF, Matérn, and RQ kernels, respectively. The hyper-tuned RBF kernel yields considerable accuracy and a reliable confidence interval.

tirely on the point with the maximum GPR predicted relative density. Conversely, a  $\lambda$  of 10 emphasizes the predicted standard deviation, giving greater weight to recipes with higher uncertainty, thereby promoting exploration in the search for optimal solutions. The process maps

are constructed based on the DOE #1 data points or DOE #1 & DOE #2 data points, as shown in Fig. 4(a–b). Thresholds to identify the conduction, transition, and keyhole melting modes are also plotted in Fig. 4 (a–b) using the temperature prediction model detailed in prior work by

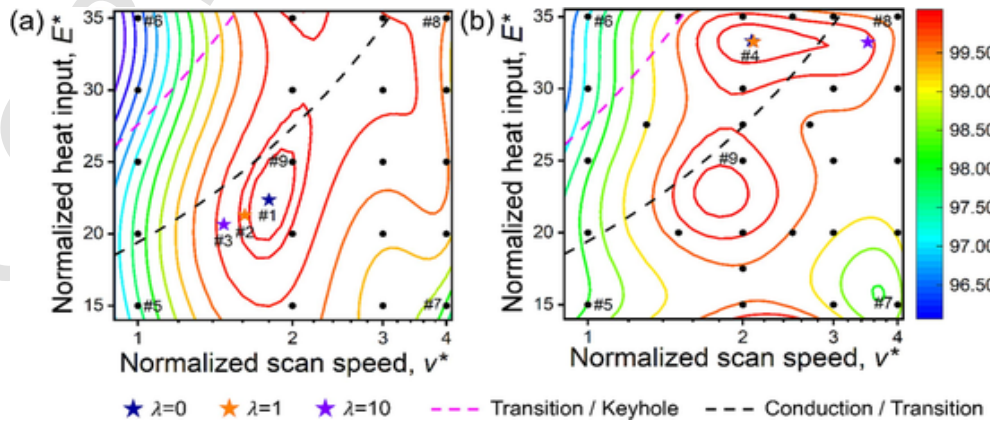


**Fig. 4.** The next optimized recipe suggested by the BO algorithm by considering different  $\lambda$  values to balance exploitation and exploration based on the (a) DOE #1 data points and (b) DOE #1 & DOE #2 data points. The results for  $\lambda$  values of 0, 1, and 10 are indicated by royal, orange, and violet stars, respectively. The conduction-transition and transition-keyhole boundaries are calculated using the melting mode model in Ref. [20], indicated by black and magenta dashed lines, respectively. (For interpretation of the references to colour in this figure legend, the reader is referred to the web version of this article.)

Patel and Vlasea [20]. The temperature prediction model used is a function of the dimensionless terms,  $E^*$  and  $v^*$ . The threshold between the conduction and transition melting modes is defined to be vaporization of  $>0.5$  times the beam spot radius used; the threshold between the transition and keyhole melting modes is defined as vaporization of  $>0.8$  times the beam spot radius into the depth of the melt pool [20].

The next suggested recipe by BO based on the different  $\lambda$  values are illustrated by royal, orange, and violet stars, respectively. It is worth mentioning that with the increase in data points, another high-density region is predicted in addition to the first high-density region already predicted by DOE #1. However, the input energy densities or even melting modes for those two regions are quite different, with the lower region belonging to the conduction mode and the upper region belonging to the transition mode. Four printing recipes suggested by the algorithm and five original DOE #1 printing recipes were selected and used to fabricate new specimens to validate the model prediction. Cylinder samples ( $\Phi 5 \times 10 \text{ mm}^3$ ) for 9 processing conditions (DOE #3) were fabricated for density measurement, as shown in Table S2. The relative densities and visualization of the three-dimensional porous defect space for all the DOE #3 samples are shown in Fig. 5. To ensure experimental

consistency, new duplicates were fabricated based on 5 DOE #1 printing recipes. The results indicate that the optimized parameters suggested by BO demonstrate good accuracy, with Sample #1 reaching a relative density of 99.97 %, which surpasses the highest relative density (Sample #9) among the previous data points. Moreover, the high relative density of Sample #4 validates that both high-density regions predicted by BO exhibit good accuracy.

Due to the sensitivity of the relative density to the hatch distance, the subsequent step is to perform inverse design (DOE #4) for low relative density samples by adjusting  $h^*$ . The goal is to predict the corresponding  $h^*$  values using a fixed combination of  $E^*$  and  $v^*$ , fabricating the samples with relative densities close to 80 %, 85 %, 90 %, and 95 %. To verify the robustness of the model, two sets of combinations of  $E^*$  and  $v^*$  were selected. The predicted  $h^*$  values and measured relative densities for the inverse design are presented in Table 3. Although there may be some disparities between the experimental results and targets, our framework could still be considered reliable and reasonably accurate, given the limited size of the dataset.

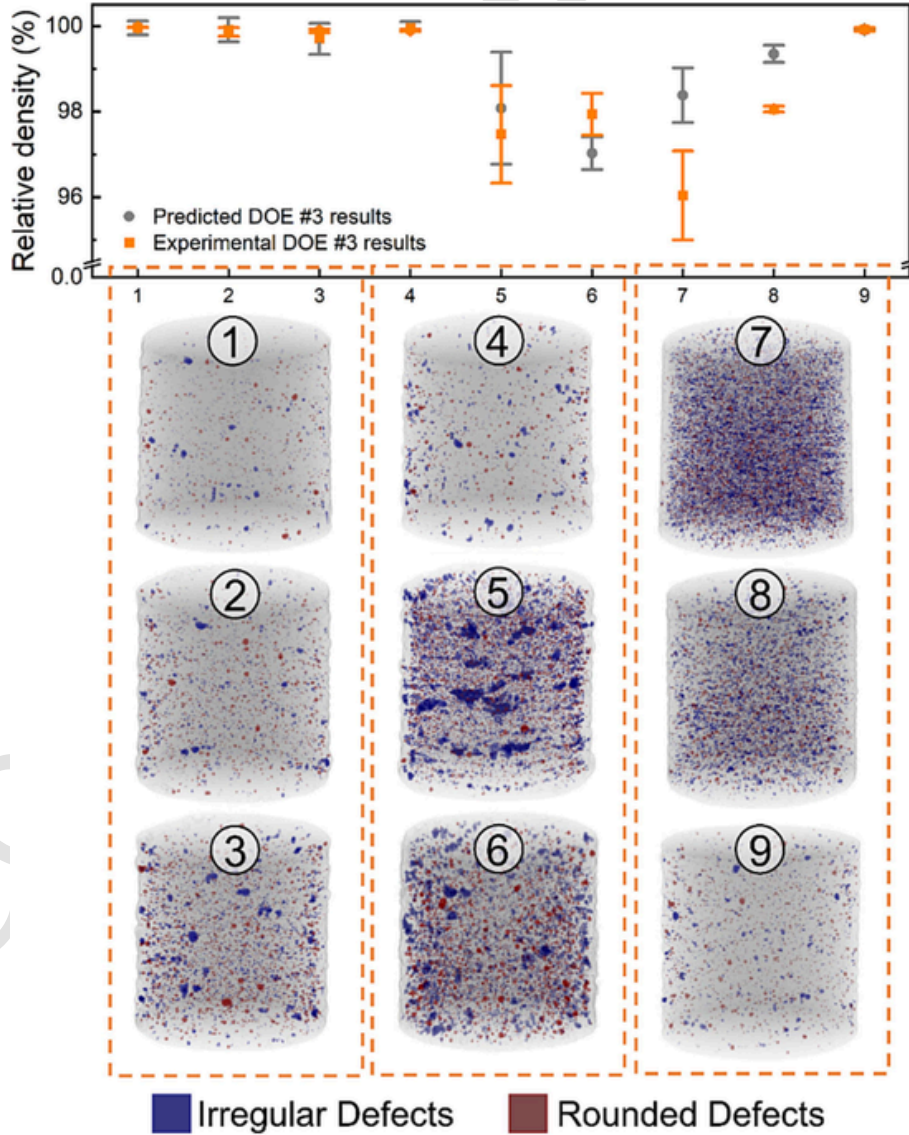


Fig. 5. The relative densities for the DOE #3 recipes compared to the predicted value from the GPR model. Defects with aspect ratios less than or equal to 0.7 were considered as irregular defects, and defects with aspect ratio  $>0.7$  were considered as rounded defects, as detailed explained in Ref. [49]. Sample #1 demonstrated enhanced performance, with a relative density of 99.97 %. The relative density of Sample #4 reaches 99.9 %, validating the accuracy of both predicted regions.

**Table 3**

The predicted  $h^*$  to fabricate samples of the target relative densities (RDs) and the experimental results for the inverse design.

| Sample label (DOE #4) | Target RD (%) | $E^*$ | $v^*$ | Predicted $h^*$ | Experimental RD (%) |
|-----------------------|---------------|-------|-------|-----------------|---------------------|
| 1                     | 95            | 22.5  | 1.8   | 4.8             | 92.39               |
| 2                     | 90            | 22.5  | 1.8   | 6.8             | 87.87               |
| 3                     | 85            | 22.5  | 1.8   | 8.69            | 84.63               |
| 4                     | 80            | 22.5  | 1.8   | 10.63           | 77.67               |
| 5                     | 90            | 25    | 2     | 6.65            | 87.84               |
| 6                     | 80            | 25    | 2     | 10.4            | 78.84               |

### 3.4. Mechanical properties and material microstructure

Table 4 shows the numerical values of relative density and hardness for the DOE #3 specimens. Furthermore, the XCT results in Fig. 5 reveal the size and distribution of pores inside the fabricated samples. Comparing Sample #4 picked from the upper high-density region to Sample #3 picked from the lower high-energy density region, the latter had a hardness almost 50 HV higher than the former, despite having a similar relative density. To elucidate the influence of grain microstructure on hardness, the EBSD inverse pole figure (IPF) of Samples #3 (Higher density), #5 (Hardest), and #7 (Highest porosity) are shown in Fig. S1(a1–a3). The grain sizes and microstructures of these samples exhibit a small difference, with an average grain size ( $d$ ) of 467, 421, and 416 nm, respectively. Similarly, as the kernel average misorientation (KAM) maps show in Fig. S1(b1–b3), the difference in local misorientations is subtle.

Tribological tests were conducted to examine the wear resistance of the low-alloy steel samples fabricated under DOE #3 printing recipes. The wear track depth, wear track width, and mean coefficients of friction (COF) values of all nine samples are summarized in Table 5, and their sectional profiles and COF profiles are depicted in Fig. S2(a–b). Sample #7 exhibited the maximum wear depth and cross-section area of 3.91  $\mu\text{m}$  and 685.1  $\mu\text{m}^2$ , respectively, whereas Sample #3 shows the minimum ones of 2.77  $\mu\text{m}$  and 239  $\mu\text{m}^2$ . These results highlight that, under the same testing conditions, Sample #7's surface was almost three times more damaged than Sample #3's surface. The COF curves of

**Table 4**

The relative density (RD) and hardness of the samples fabricated using the recipes in DOE #3.

| Sample label (DOE #3) | RD (%)           | Hardness (HV <sub>0.2</sub> ) |
|-----------------------|------------------|-------------------------------|
| 1                     | 99.97 $\pm$ 0.01 | 450 $\pm$ 20                  |
| 2                     | 99.86 $\pm$ 0.1  | 493 $\pm$ 12.5                |
| 3                     | 99.89 $\pm$ 0.04 | 512 $\pm$ 25                  |
| 4                     | 99.9 $\pm$ 0.03  | 443 $\pm$ 6                   |
| 5                     | 97.47 $\pm$ 1.14 | 556 $\pm$ 29                  |
| 6                     | 97.94 $\pm$ 0.49 | 490 $\pm$ 31                  |
| 7                     | 96.04 $\pm$ 1.04 | 474 $\pm$ 5.8                 |
| 8                     | 98.06 $\pm$ 0.07 | 465 $\pm$ 27                  |
| 9                     | 99.92 $\pm$ 0.04 | 449 $\pm$ 30                  |

**Table 5**

The wear track depth, width, and mean coefficients of friction (COF) values of samples fabricated using the recipes in DOE #3.

| Sample label (DOE #3) | Width ( $\mu\text{m}$ ) | Depth ( $\mu\text{m}$ ) | Mean COF |
|-----------------------|-------------------------|-------------------------|----------|
| 1                     | 0.257                   | 3.92                    | 0.491    |
| 2                     | 0.292                   | 3.26                    | 0.423    |
| 3                     | 0.250                   | 2.77                    | 0.424    |
| 4                     | 0.293                   | 4.26                    | 0.439    |
| 5                     | 0.285                   | 4.57                    | 0.453    |
| 6                     | 0.336                   | 4.42                    | 0.436    |
| 7                     | 0.341                   | 3.91                    | 0.449    |
| 8                     | 0.302                   | 3.65                    | 0.413    |
| 9                     | 0.285                   | 4.05                    | 0.417    |

all samples decrease rapidly in the initial running-in stage, then stabilize after 600 s, as shown in Fig. S2(b). Sample #5 exhibits the highest mean COF due to its highest hardness, leading to the highest shear stress between the surfaces.

Six samples were selected to conduct a detailed comparison of wear track characteristics: Sample #1 (most dense), Sample #3 (best-performing), Sample #4 (transition mode), Sample #5 (hardest), Sample #7 (worst-performing) and Sample #9 (best original recipe). Fig. 6 (a1–a3) show the SEM images of the worn surfaces of Samples #3, #5, and #7 after the sliding test, revealing sliding grooves and detachments on the surface of the glaze layer due to severe abrasive wear and adhesive wear. With the decrease in the relative density, the area of the glaze layer becomes more and more intact. The contrasting wear performance observed in Sample #1, Sample #4, and Sample #9 demonstrate the decisive influence of hardness, when relative densities are similar. In comparison with Sample #4, a reduction in the wear track width is observed in both Sample #1 and Sample #9, as shown in Fig. 6(b1–b3).

To further quantify the tribological performance of DOE #3 samples, the specific wear rate is calculated by the following formula [30]:

$$\text{Wear rate} = \frac{\text{Volume (mm}^3\text{)}}{\text{Load (N)} * \text{Total distance (m)}} \quad (10)$$

From the typical Archard equation [31], it is evident that the wear volume of the material is inversely proportional to hardness, meaning that a harder sample would exhibit better wear resistance. Aminul and Zoheir further noted that the amount, size, and shape of pores significantly influence material removal during wear [32]. To gain insight into the wear difference of various samples, Fig. 7 shows the results of relative densities, hardness, and specific wear rates of all samples. The wear performances of Samples #1, #2, #3, and #4 prove that hardness is the determining factor when relative densities are similar. On the other hand, the poor wear performance of Sample #5 is attributed to its high porosity. Lower hardness and the highest porosity result in the worst wear performance of Sample #7.

## 4. Discussion

### 4.1. Machine learning model for establishing the process map and optimizing the printing recipe

In the LPBF process, establishing a parameter-property map to control and optimize the sample quality is crucial yet challenging. There are dozens of controllable printing parameters impacting the sample quality, moreover, the consistency of the experimental results would be further affected by using unconventional material systems such as non-equiaxed metal powders. In this study, assisted by the GPR model, we systematically established a  $P$ - $v$  process map within a practical processing space for low-alloy steel. After establishing the accurate 2D process map, hatch distance is the third factor to be determined and controlled for designing low relative density samples. By the inverse design strategy, our framework generates a reliable 3D processing window based on limited experimental data points for predicting desired printing recipes. Furthermore, the BO algorithm is employed to find the optimized recipe of  $E^*$  and  $v^*$  from previously unexplored printing recipes, with three  $\lambda$  values chosen to balance exploitation and exploration. Four optimized printing recipes suggested by BO are selected and applied for the fabrication of low-alloy steel samples to validate the accuracy of the models, as shown in Fig. 5.

Based on the established processing window derived from DOE #1 data points, a high-density region is identified around the [1.8, 22.5] points, which belongs to the conduction mode. The stable heat conduction within the melting pool is the main reason for reduced porosity formation. Conversely, the second high-density region detected by the DOE #1 & DOE #2 data points is located in the transition mode, characterized by higher energy input. Zhao's research has shown that exces-



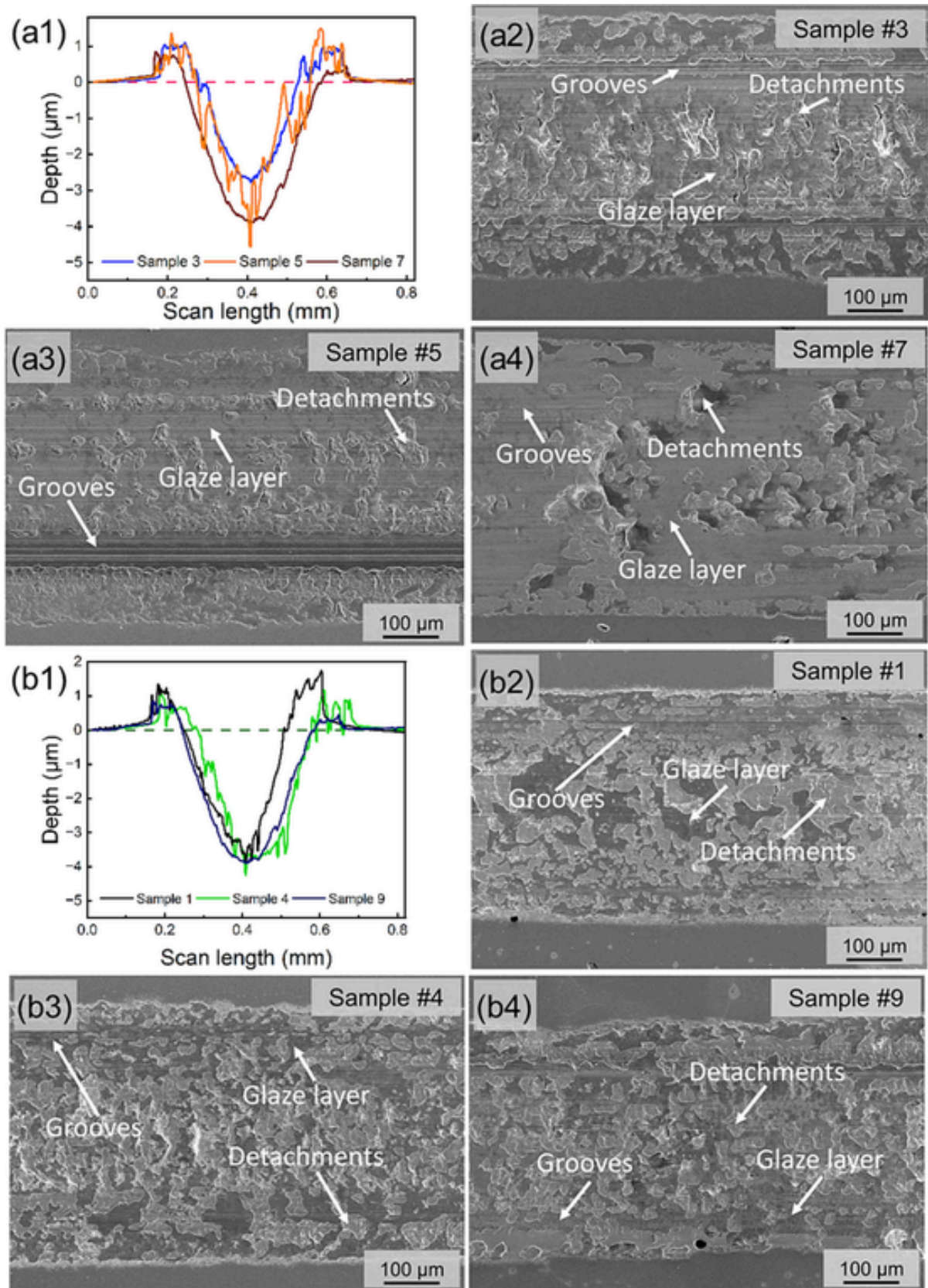


**Fig. 6.** The (a1) sectional profile of wear tracks of Sample #3, Sample #5, and Sample #7, along with (a2–a4) their corresponding SEM images. The (b1) sectional profile of wear tracks of Sample #1, Sample #4, and Sample #9, along with (b2–b4) their corresponding SEM images. The difference in wear track characteristics among these samples indicates that relative density and hardness are two influential impacts on wear performance.

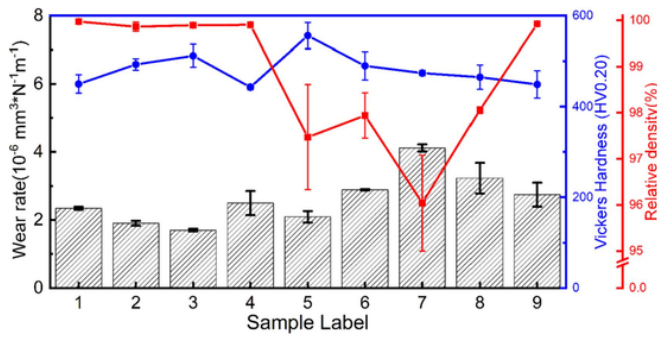


Fig. 7. The hardness, relative density, and specific wear rate of LPBF fabricated low-alloy steel samples. The results showed that higher hardness and relative density contribute to increased wear resistance.

sive input energy, induced by high power and lower speed in LPBF processes, leads to keyhole porosity [33]. In contrast, Hojjatzadeh's work [34] has demonstrated that a high thermocapillary force induced by a high-temperature gradient could eliminate pores from the melting pool. Therefore, we hypothesize that the second high-density region is the outcome of a delicate balance between keyhole fluctuation and porosity elimination mechanisms. Importantly, the strength of deploying the BO algorithm is in identifying processing windows (conduction and transition mode for this material system) with similar density response but expected to have different microstructure and mechanical properties as elucidated in this study.

#### 4.2. Tribological behavior and mechanism analysis

Previous publications suggest that hardness and relative density are the two main factors to identify suitable candidates for wear applications [31,35]. One common way to reinforce the wear performance of LPBF fabricated steels is to incorporate dispersed secondary phase hard particles or stronger fillers into the metal matrix, forming metal matrix composites (MMCs) [36]. However, the mixture of hard particles would cause the accumulation of high residual stress, inducing crack initiation and propagation which in turn could be detrimental to the wear performance of samples. Moreover, the addition of hard ceramic particles will increase the processing cost and pose challenges for widespread adoption.

In this study, we have found the LPBF low-alloy steel to be a suitable candidate for automotive gears due to its low cost and exceptional wear performance. To determine the best recipes for fabricating samples with improved wear resistance, we involved initially employing a data-driven framework to identify high-density regions within the design space. Subsequently, we selected the recipes that yield improved hardness within these regions. Among all the samples, Sample #3 demonstrated the best wear resistance, which is attributed to the improvement of relative density while maintaining a high hardness. As summarized in Fig. 8, our optimized samples from both conduction mode and transition mode demonstrate superior wear performance compared with un-optimized samples and high-density samples from the literature [27,37–45], including various LPBF fabricated steel and MMCs. Notably, although our samples are not as hard as other materials, they still yield exceptional wear performances. For further explanation, the strengthening mechanism is discussed in detail below.

The crucial reason for the exceptional wear resistance is the in-situ oxidation behavior exhibited by the modified low-alloy steel powders. Yang et al., [46] proved that the as-received powders are susceptible to oxidation at low temperatures ( $< 560^{\circ}\text{C}$ ). Similar characteristics is further confirmed by our EDS mapping results, where the oxygen content increased from 0.056 % in the virgin powder to approximately 2.5 % on the as-build sample surface, and eventually reaching  $> 20$  % on the glaze layer of the worn surface. The first stage of oxygen content change

is associated with the limited formation of an oxidation film prior to testing. During the early stages of sliding, this film broke down rapidly, leading to metal-metal contact. This, in turn, causes a high COF, which generates significant frictional heat that promotes the reaction between Fe and O present in the environment, facilitating the second stage of oxidation, which is more pronounced. SEM images and EDS mapping analysis were used to examine the wear track of Sample #5, revealing a significant amount of oxidation on the surface of glaze layers, as shown in Fig. 9. High oxygen content on the glaze layer indicates that the counterpart interacts with the oxide layer on the surface instead of the alloy beneath, which helps reduce friction on the surface. Similar oxygen enrichment on the surface of the glaze layer is also characterized in Sample #4 and Sample #9 by EDS point scanning, as shown in Fig. S3. Furthermore, the formation of oxides results in enhanced adhesion between the samples surface and the counterpart, as evidenced by the consistent patterns observed in the element distributions of O and W in the EDS mapping results [47]. The strong adhesion could be one main reason for the detachments on the worn surface shown in Fig. 6. In low-density samples, another cause for the release of wear particles is fatigue wear. The pores inside the sample serve as initiators for crack growth and a secondary crack might subsequently emerge from a primary crack, propagating until it reaches the primary crack again and culminates in the formation of a wear particle. These mechanisms are extensively elaborated upon by Stachowiak and Batchelor [48]. The existence of nearly detached wear particles and the presence of cracks in the high-magnification SEM images validate the involvement of fatigue wear, as illustrated in Fig. 10.

#### 5. Conclusion

In this study, we have successfully developed a data-driven based framework to design and optimize the sample density and wear resistance of an LPBF-fabricated low-alloy steel. To that end, we generate a 3D process window regarding main printing parameters (i.e., laser power, scan speed, and hatch distance) and the relative density of samples by employing the strategies of the GPR, BO, and inverse design:

1. To establish a more precise  $P$ - $v$  process map, we trained and hyper-tuned the GPR model using various kernel functions, ultimately selecting the RBF kernel with an RMSE of 0.136. We selected three  $\lambda$  values for the BO algorithm to strike a balance between the exploitation and exploration in identifying the globally optimal processing parameters within the established process map. Additionally, since the relative density is the most sensitive to changes in hatch distance, the inverse design strategy is employed to predict the corresponding hatch distance to fabricate the target low-density samples.
2. The relative density of the sample fabricated by our best-optimized recipe is 99.97 %, surpassing the highest relative density among all the samples. Furthermore, all the samples fabricated using the suggested optimized recipes exhibited high relative density, thus validating the accuracy of the two GPR-predicted high-density regions and corresponding to the conduction mode and transition mode, respectively.
3. The samples fabricated by our optimized parameters demonstrated enhanced relative density and retain a high hardness, resulting in a superior wear rate compared to those produced using non-optimized parameters. Furthermore, our samples outperform LPBF-fabricated steels and metal matrix composites in the literature, which is attributed to the existence of oxidative and fatigue wear.

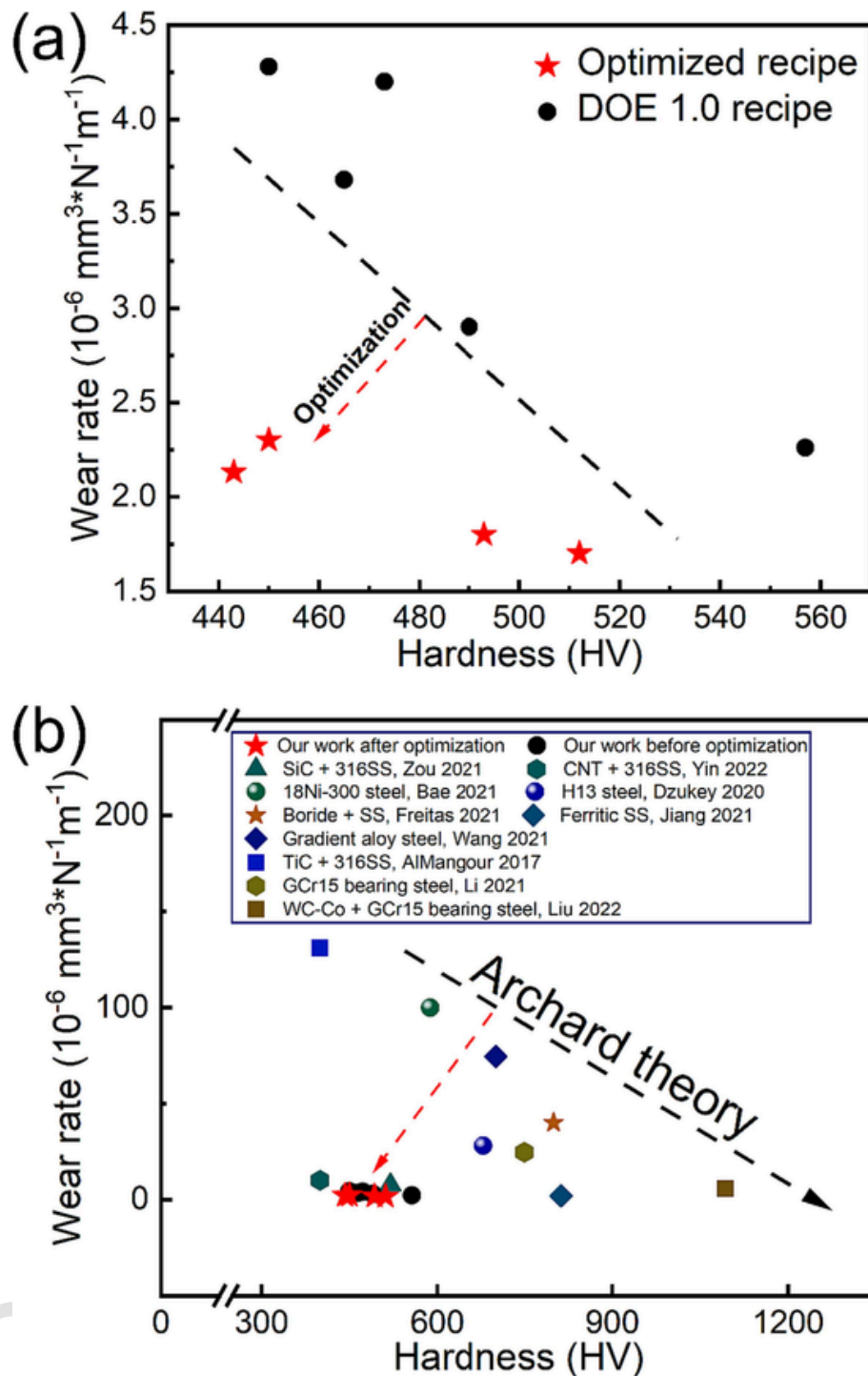


**Fig. 8.** Specific wear rates of (a) optimized samples compared with the original samples and (b) our work compared to those reported in literature [27,37–45]. Although the raw LPBF fabricated samples showed significant wear resistance, parameter optimization further leverages the material's potential.

#### Declaration of competing interest

The authors declare that they have no known competing financial interests or personal relationships that could have appeared to influence the work reported in this paper.

#### Acknowledgements

J.Z and Y.Z acknowledge the financial support from Natural Sciences and Engineering Research Council of Canada (NSERC Discovery

Grant # RGPIN-2018-05731), the Centre for Analytics and Artificial Intelligence Engineering (CARTE) Seed Funding program, New Frontiers in Research Fund-Exploration (NFRFE-2019-00603), Data Sciences Institute Catalyst Grant, and NSERC Alliance Grants—Missions ALLRP 570708-2021. S.P. and M.V. appreciate the funding support received from Federal Economic Development Agency for Southern Ontario (FedDev Ontario grant # 814654), Canada, in partnership with Rio Tinto QMP, Sorel-Tracy, QC, and Miba Sinter Austria GmbH, Laakirchen, Austria. The authors would like to acknowledge the contribution of Rio Tinto for their support with providing metal powder and



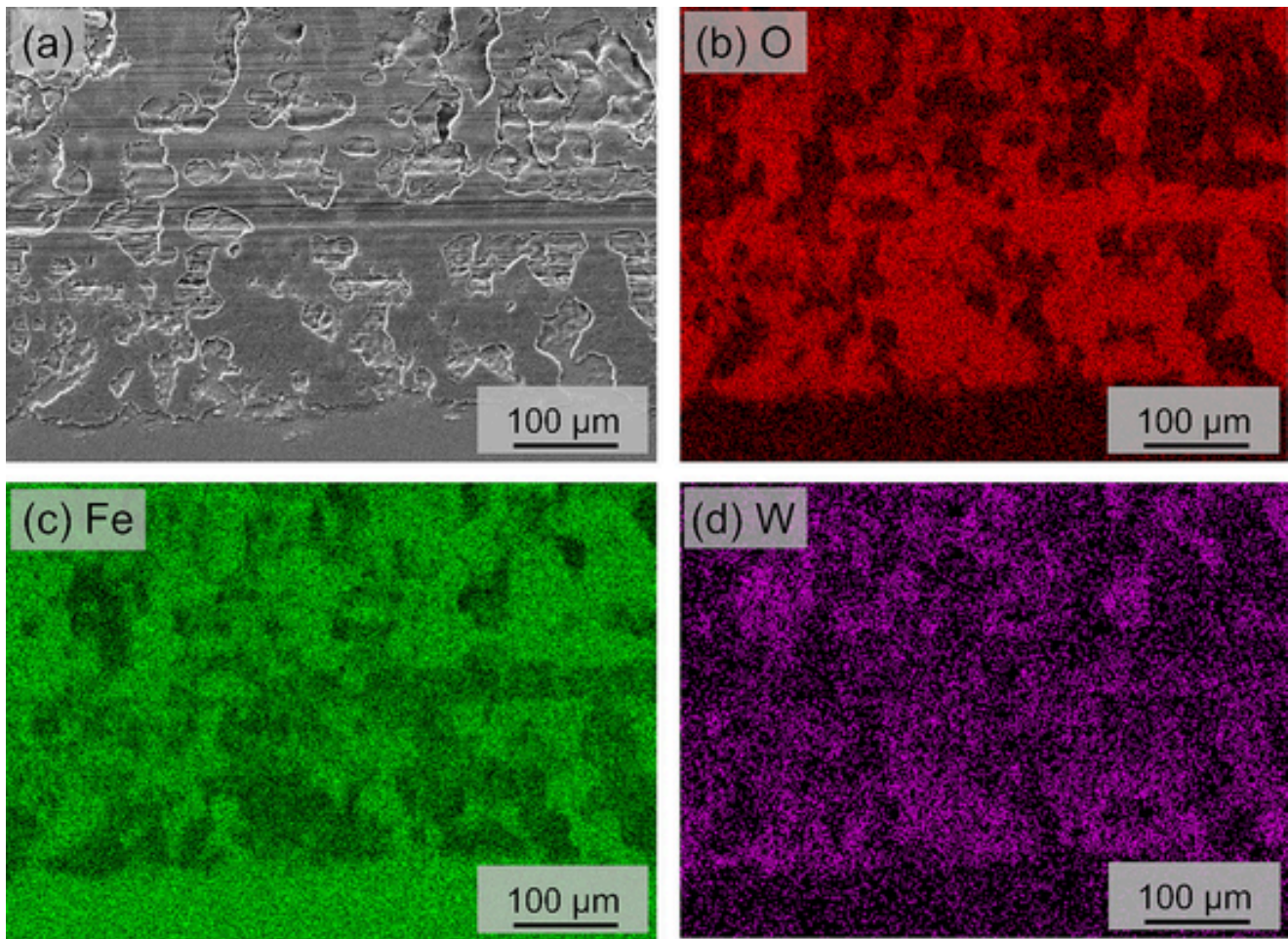


**Fig. 9.** The EDS mapping results of a selected portion of the wear track in Sample #5. The abundance of O confirms the presence of oxidative wear, resulting in the superior wear performance. Additionally, the pattern of W indicates a strong adhesion between the counterpart and the sample surface.

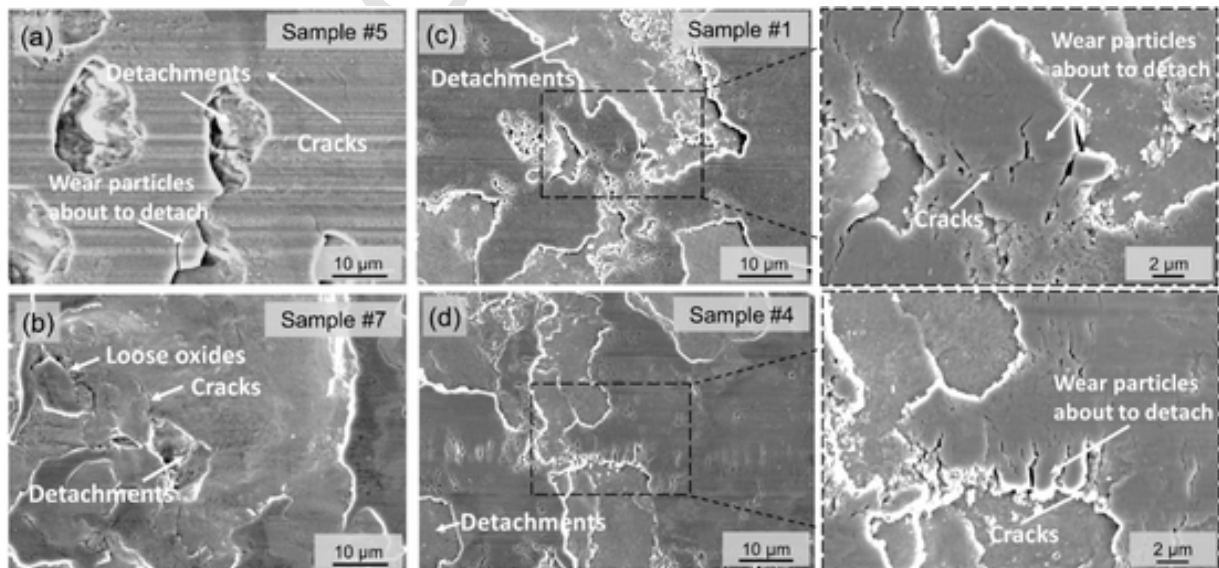


**Fig. 10.** The high magnification SEM images of the internal features of the wear tracks in (a) Sample #5, (b) Sample #7, (c) Sample #1, and (d) Sample #4. The zoom-in of selected black rectangular regions shows more details about surface cracks that cause fatigue wear, leading to the detachment of wear particles.

LECO analysis. The authors acknowledge the detailed material information on low-alloy steel provided by M. Yang from the University of Waterloo.



## Appendix A. Supplementary data

Supplementary data to this article can be found online at <https://doi.org/10.1016/j.jmapro.2024.01.083>.

## References

- [1] Davis J.R. Surface engineering for corrosion and wear resistance. ASM international; 2001.
- [2] Chattopadhyay R. Surface wear: Analysis, treatment, and prevention. ASM international; 2001.
- [3] Venetacci S, Ponticelli G.S, Guarino D, Guarino S. Tribological properties of laser powder bed fused AlSi10Mg: experimental study and statistical analysis. *Journal of Manufacturing Processes* 2022;84:1103–21.
- [4] Gachot C, Rosenkranz A, Hsu S.M, Costa H.L. A critical assessment of surface texturing for friction and wear improvement. *Wear* 2017;372:21–41.
- [5] Deshpande P.K, Lin R.Y. Wear resistance of WC particle reinforced copper matrix composites and the effect of porosity. *Mater Sci Eng A* 2006;418:137–45.
- [6] King W.E, Anderson A.T, Ferencz R.M, Hodge N.E, Kamath C, Khairallah S.A, et al. Laser powder bed fusion additive manufacturing of metals; physics, computational, and materials challenges. *Appl Phys Rev* 2015;2:041304.
- [7] DeRoy T, Mukherjee T, Wei H.L, Elmer J.W, Milewski J.O. Metallurgy, mechanistic models and machine learning in metal printing. *Nature Reviews Materials* 2021;6:48–68.
- [8] Oliveira J.P, LaLonde A.D, Ma J. Processing parameters in laser powder bed fusion metal additive manufacturing. *Materials & Design* 2020;193:108762.
- [9] Stopyna W, Gruber K, Smolina I, Kurzynowski T, Kuźnicka B. Laser powder bed fusion of AA7075 alloy: influence of process parameters on porosity and hot cracking. *Addit Manuf* 2020;35:101270.
- [10] Taherkhani K, Ero O, Liravi F, Toorandaz S, Toyserkani E. On the application of in-situ monitoring systems and machine learning algorithms for developing quality assurance platforms in laser powder bed fusion: a review. *Journal of Manufacturing Processes* 2023;99:848–97.
- [11] Letenneur M, Kreitzberg A, Brailovski V. Optimization of laser powder bed fusion processing using a combination of melt pool modeling and design of experiment approaches: density control. *Journal of Manufacturing and Materials Processing* 2019;3:21.
- [12] Knaak C, Masseling L, Duong E, Abels P, Gillner A. Improving build quality in laser powder bed fusion using high dynamic range imaging and model-based reinforcement learning. *IEEE Access* 2021;9:55214–31.
- [13] Liu J, Ye J, Momin F, Zhang X, Li A. Nonparametric bayesian framework for material and process optimization with nanocomposite fused filament fabrication. *Addit Manuf* 2022;54:102765.
- [14] Maleki E, Bagherifard S, Guagliano M. Application of artificial intelligence to optimize the process parameters effects on tensile properties of Ti-6Al-4V fabricated by laser powder-bed fusion. *International Journal of Mechanics and Materials in Design* 2021;1–24.
- [15] Guo L, Liu H, Wang H, Wei Q, Zhang J, Chen Y, et al. A high-fidelity comprehensive framework for the additive manufacturing printability assessment. *Journal of Manufacturing Processes* 2023;105:219–31.
- [16] La Fé-Perdomo I, Ramos-Grez J.A, Jeria I, Guerra C, Barrionuevo G.O. Comparative analysis and experimental validation of statistical and machine learning-based regressors for modeling the surface roughness and mechanical properties of 316L stainless steel specimens produced by selective laser melting. *Journal of Manufacturing Processes* 2022;80:666–82.
- [17] Liu Q, Wu H, Paul M.J, He P, Peng Z, Gludovatz B, et al. Machine-learning assisted laser powder bed fusion process optimization for AlSi10Mg: new microstructure description indices and fracture mechanisms. *Acta Mater* 2020;201:316–28.
- [18] He P, Liu Q, Kruzic J.J, Li X. Machine-learning assisted additive manufacturing of a TiCN reinforced AlSi10Mg composite with tailorable mechanical properties. *Mater Lett* 2022;307:131018.
- [19] Thomas M, Baxter G.J, Todd I. Normalised model-based processing diagrams for additive layer manufacture of engineering alloys. *Acta Mater* 2016;108:26–35.
- [20] Patel S, Vlasea M. Melting modes in laser powder bed fusion. *Materialia* 2020;9:100591.
- [21] Ye J, Khairallah S.A, Rubenchik A.M, Crumb M.F, Guss G, Belak J, et al. Energy coupling mechanisms and scaling behavior associated with laser powder bed fusion additive manufacturing. *Adv Eng Mater* 2019;21:1900185.
- [22] Mockus J. Bayesian approach to global optimization: Theory and applications. Springer Science & Business Media; 2012.
- [23] J. Snoek, H. Larochelle, R.P.J.A.i.n.i.p.s. Adams, Practical bayesian optimization of machine learning algorithms, 25 (2012).
- [24] Williams C.K, Rasmussen C.E. Gaussian processes for machine learning. MA: MIT press Cambridge; 2006.
- [25] Astm E. Standard test methods for Vickers hardness and Knoop hardness of metallic materials, west Conshohocken. ASTM International: PA; 2017.
- [26] G.J.S.T.M.f.L.R.B.-o.-F.S.W. Astm, Annual Book of ASTM Standards, 133–05, 3 (2005).
- [27] Dzukey G.A, Yang K, Wang Q, Zhuang B, Hou W. Porosity, hardness, friction and wear performance analysis of H13 SLM-formed samples. *J Mater Eng Perform* 2020;29:4957–66.
- [28] Maodzeka D.K, Olakanmi E.O, Mosalagae M, Hagedorn-Hansen D, Pityana S.L. Hybrid optimisation studies on the microstructural properties and wear resistance of maraging steel 1.2709 parts produced by laser powder bed fusion. *Optics & Laser Technology* 2023;159:108914.
- [29] Li X, Liu Y, Zhou Z. Influence of hatch distance on processing, microstructure and mechanical properties of AlMgScZr alloy fabricated by laser powder bed fusion. *Journal of Manufacturing Processes* 2022;81:78–91.
- [30] Zhang K, Shi X, Xue Y, Huang Q, Wu C. Effects of composite textured surface on friction characteristics of 42CrMo steel under grease lubrication. *Wear* 2022;504:204419.
- [31] Archard J. Contact and rubbing of flat surfaces. *J Appl Phys* 1953;24:981–8.
- [32] Islam M.A, Farhat Z.N. Effect of porosity on dry sliding wear of Al–Si alloys. *Tribology International* 2011;44:498–504.
- [33] Zhao C, Parab N.D, Li X, Fezzaa K, Tan W, Rollett A.D, et al. Critical instability at moving keyhole tip generates porosity in laser melting. *Science* 2020;370:1080–6.
- [34] Hojjatzadeh S.M.H, Parab N.D, Yan W, Guo Q, Xiong L, Zhao C, et al. Pore elimination mechanisms during 3D printing of metals. *Nat Commun* 2019;10:3088.
- [35] Dubrujeaud B, Vardavoulas M, Jeandin M. The role of porosity in the dry sliding wear of a sintered ferrous alloy. *Wear* 1994;174:155–61.
- [36] Dadkhah M, Mosallanejad M.H, Iuliano L, Saboori A. A comprehensive overview on the latest progress in the additive manufacturing of metal matrix composites: potential, challenges, and feasible solutions. *Acta Metallurgica Sinica (English Letters)* 2021;34:1173–200.
- [37] Jiang P.F, Zhang C.H, Zhang S, Zhang J.B, Chen J, Chen H.T. Additive manufacturing of novel ferritic stainless steel by selective laser melting: role of laser scanning speed on the formability, microstructure and properties. *Optics & Laser Technology* 2021;140:107055.
- [38] Zou Y, Tan C, Qiu Z, Ma W, Kuang M, Zeng D. Additively manufactured SiC-reinforced stainless steel with excellent strength and wear resistance. *Addit Manuf* 2021;41:101971.
- [39] Yin H, Yang J, Zhang Y, Crilly L, Jackson R.L, Lou X. Carbon nanotube (CNT) reinforced 316L stainless steel composites made by laser powder bed fusion: microstructure and wear response. *Wear* 2022;496:204281.
- [40] Bae K, Kim D, Lee W, Park Y. Wear behavior of conventionally and directly aged maraging 18Ni-300 steel produced by laser powder bed fusion. *Materials* 2021;14:2588.
- [41] Wang X, Zhang C.H, Cui X, Zhang S, Chen J, Zhang J.B. Novel gradient alloy steel with quasi-continuous ratios fabricated by SLM: material microstructure and wear mechanism. *Mater Charact* 2021;174:111020.
- [42] AlMangour B, Grzesiak D, Yang J.-M. In-situ formation of novel TiC-particle-reinforced 316L stainless steel bulk-form composites by selective laser melting. *J Alloys Compd* 2017;706:409–18.
- [43] Freitas B.J.M, de Oliveira V.A, Gargarella P, Koga G.Y, Bolfarini C. Microstructural characterization and wear resistance of boride-reinforced steel coatings produced by selective laser melting (SLM). *Surf Coat Technol* 2021;426:127779.
- [44] Li Y, Liu S, Xue T, Wei Y, Yang X, Wang Y. Comparison of wear behavior of GCr15 bearing steel prepared by selective laser melting (SLM) and electron beam melting (EBM). *Mater Lett* 2021;305:130726.
- [45] Liu S, Li Y, Wang Y, Wei Y, Zhang L, Wang J. High wear resistance WC-co reinforced GCr15 bearing steel composite prepared via selective laser melting (SLM). *Int J Refract Met Hard Mater* 2022;109:105988.
- [46] M. Yang, M.K. Keshavarz, M.L. Vlasea, A. Molavi-Kakhki, L. Martin, Supersolidus Liquid Phase Sintering of Water-Atomized Low-Alloy Steel in Binder Jetting Additive Manufacturing, Available at SSRN 4283080.
- [47] Williams J. Engineering tribology. Cambridge University Press; 2005.
- [48] Stachowiak G.W, Batchelor A.W. Engineering tribology. Butterworth-heinemann; 2013.
- [49] Patel S, Chen H, Vlasea M, Zou Y. The influence of beam focus during laser powder bed fusion of a high reflectivity aluminium alloy—AlSi10Mg. *Addit Manuf* 2022;59:103112.